Appl. Phys. A (2015) 118:931–938
DOI 10.1007/s00339-014-8816-2

**Applied Physics A**
**Materials Science & Processing**

# Effect of fabrication routes on the microstructure, the dielectric and ferroelectric properties of the Mn-doped $BaTiO_3$ ceramics

**Xia Zhao · Wei Chen · Lixue Zhang · Jinghui Gao · Lisheng Zhong**

Received: 19 June 2014 / Accepted: 5 October 2014 / Published online: 20 November 2014


**Abstract** The effect of fabrication routes on the microstructure, the dielectric and ferroelectric properties of the Mn-doped $BaTiO_3$ ceramics was systematically studied in the present study. It can be concluded that the ways of doping manganese into $BaTiO_3$ matrix had a strong impact on the obtained ceramics. Doping manganese after the calcination of $BaTiO_3$ (BT + Mn) would inhibit the grain growth and cause the hexagonal $BaTiO_3$ when sintered at 1,400 °C in the air. While doping manganese at the initial stage [$BaTi_{(1-x)}Mn_xO_3$], no hexagonal $BaTiO_3$ is detected in the same sintering temperature. As the macroscopic properties, the dielectric properties showed permittivity diffusion with the frequency in the temperature range of −10 to 150 °C only in the ceramics fabricated by the former route (BT + Mn). Moreover, the dielectric relaxation process disappeared after aging treatment only in the ceramics fabricated by the later route [$BaTi_{(1-x)}Mn_xO_3$]. The ferroelectric properties showed strong aging effect in the sample fabricated by the latter route [$BaTi_{(1-x)}Mn_xO_3$] both with fine grain and coarse grain, while the sample fabricated by the former route (BT + Mn) showed slight aging phenomenon ever after aging at room temperature for 10 days. The electrostrain also showed big difference within different samples: The recoverable electrostrain were 0.11 % (BT + Mn) and 0.21 % [$BaTi_{(1-x)}Mn_xO_3$] at the same sintering temperature of 1,320 °C and aging in the room temperature for 10 days. Such results were analyzed from the viewpoint of the differences in solubility of manganese and the consequent manganese–oxygen vacancy defect dipoles in the different fabrication routes.

X. Zhao · W. Chen (✉)
School of Electrical Engineering, Xi'an Jiaotong University, Xi'an 710049, China
e-mail: weic@mail.xjtu.edu.cn

L. Zhang
State Key Laboratory for Mechanical Behavior of Materials, Xi'an Jiaotong University, Xi'an 710049, China

J. Gao · L. Zhong
State Key Laboratory of Electrical Insulation and Power Equipment, Xi'an Jiaotong University, Xi'an 710049, China

## 1 Introduction

$BaTiO_3$ is one of the most widely used ferroelectric materials for its high performance in dielectric, ferroelectric and piezoelectric properties [1, 2]. In order to tailor the properties, various doping is inevitably necessary. Manganese, as an acceptor dopant, is usually used to improve the properties of the $BaTiO_3$-based ceramics. Microstructure and electrical properties of Mn-doped $BaTiO_3$ have been extensively studied by numerous researchers [3–15]. For the donor-doped positive temperature coefficient of resistance (PTCR) ceramics, manganese depresses the grain size and enhances the electrical resistivity near the Curie temperature of $BaTiO_3$ [16–23]. For the based-metal-electrode (BME) MLCCs, undoped-perovskite $BaTiO_3$ materials are reduced and become semiconductors when fired in the protective atmosphere which is to prevent the internal electrodes from being oxidized. But doping of manganese is an effective way to prevent the degradation of insulation resistance and to extend the service life of MLCCs [24–26]. In order to improve life stability of BME-MLCCs, manganese always doped mix with donors [27]. Manganese is also used to stabilize hexagonal $BaTiO_3$ (h-$BaTiO_3$) at room temperature [28–34]. Recent studies indicate a new effect in the Mn-doped $BaTiO_3$ ceramic; it can generate a large recoverable electrostrain after the aging treatment [35–38].

For the above-mentioned applications of the Mn-doped $BaTiO_3$ ceramics, the doping ways and the consequent effects of manganese are not quite the same. For the PTCR studies, the key role of manganese in PTCR ceramics is to modify the grain boundary layer characteristics while keeping the grain-bulk conductive; a small addition of 0.04 at. % of manganese can result in increasing the height of the grain boundary potential barriers by $\sim$40 % in the temperature range between $T_C$ and $T_{max}$ [23]. In this study, the manganese was added at the first stage into $BaCO_3$ and $TiO_2$ and then calcined. For the Mn-doped MLCC studies [24–26], the authors doped manganese into the $BaTiO_3$ and found that manganese segregated along the grain boundary, which improved the insulation resistance in the reducing-atmosphere-sintered MLCCs [26]. For the dopant mixes of acceptors and donors to improve life stability of BME-MLCCs, re-oxidation treatment at 800 $\pm$ 1,100 °C was needed. Re-oxidation of Mn-acceptor-doped $BaTiO_3$ ceramics leads to a valence change of $Mn^{2+}$ to $Mn^{3+}$ or even $Mn^{4+}$ [39]. The number of oxygen vacancies necessary to compensate the acceptors is considerably diminished by re-oxidation. Donors are capable of compensating the acceptors in place of oxygen vacancies. Donors and acceptors are assumed to form complexes. The mobility of donor–acceptor complexes in the electric field is reported as extremely low [40]. However, for this study, the doping ways of manganese are not quite the same. In Kishi's [41] and Albertsen's [42] studies, the manganese was added at the first stage into $BaCO_3$ and $TiO_2$ and then calcined, while in Wang's study, the authors doped manganese into the $BaTiO_3$ [43]. Abicht et al. reported that 0.5–1.7 mol % Mn-doped $BaTiO_3$ ceramics sintered at 1,400 °C in air exhibited abnormal hexagonal crystallographic structure at room temperature which is different from the conventional tetragonal structure. It can cause a drastic change in the microstructure. For their study, the manganese was added at the first stage into $BaCO_3$ and $TiO_2$ and then calcined [34]. For the studies of the favorable properties of aging by generating the large recoverable strain [35–38], the manganese was added at the first stage into $BaCO_3$ and $TiO_2$ and then calcined. However, comparing the published results, the overall picture of the influence of doping ways of manganese as well as their different effects on their dielectric and ferroelectric properties are not clear.

Hence, the aim of this paper was to clarify the influence of fabrication routes on the microstructure, the dielectric and ferroelectric properties of the Mn-doped $BaTiO_3$ ceramics. Here we employed two ways of doping manganese into $BaTiO_3$ matrix, i.e., doping manganese at the initial stage and after the calcination of $BaTiO_3$. The different consequent effect on the microstructures and dielectric/ferroelectric properties of $BaTiO_3$ ceramics by equal mole of manganese are investigated. The paper is arranged in the following way: The Mn-doped $BaTiO_3$ ceramics with different preparation routes was firstly described; their microstructures were detected by X-ray diffraction (XRD) and scanning electron microscopy (SEM); and the dielectric properties with the change of temperature and the dielectric relaxation behavior in ferroelectric tetragonal phase were then studied. The ferroelectric properties as well as the aging behavior with different doping ways were also studied.

## 2 Experimental procedures

Commercially available high-purity $BaCO_3$ (99.9 %, Zhan Peng, Hubei, China, $d_{50} = 400$ nm) and $TiO_2$ (99.9 %,Rutile, Zhan Peng, Hubei, China, $d_{50} = 220$ nm) were used as the starting materials as well as the analytically pure $MnCO_3$. The two fabrication routes were described as follows: (1) $BaTiO_3$ (abbreviated as BT) was firstly synthesized at 1,200 °C for 2 h and then mixed with 0.65 mol % of Mn dopant; (2) the manganese dopant was added at the initial stage with $BaCO_3$ and $TiO_2$ and then calcined at 1,200 °C for 2 h, the doping amount is 0.65 mol %. The route 1 and route 2 abbreviated as BT + Mn and $BaTi_{(1-x)}Mn_xO_3$ ($x = 0.0065$). Both the calcinated powder was milled for 8 h with zirconium balls of 6 mm in diameter. The dried powder was added PVA aqueous solution and then pressed into pellets with the diameter of 12.56 mm and the thickness of 1.5 mm. Sintering was done from 1,260 to 1,400 °C with the same holding time of 2 h in air. The sample volume density was determined by the Archimedes method. The phase composition of the samples was obtained using X-ray diffractometry, and the powder diffraction data were collected at room temperature between $20 \leq 2\theta \leq 80$ in step of 0.02° using an X-ray diffractometer (SHIMADZU XRD7000). The scanning electron microscope (SEM, KEYENCE VE-9800) was used for the characterization of grain morphology. In order to measure the dielectric and ferroelectric properties, silver paste was coated on both surfaces of the ceramics and then fired at 800 °C for 40 min. For the aging study, the samples were de-aged by exposed to 300 °C for 0.5 h and then furnace cooling to the room temperature then suffered the aging treatment, while the unaged sample was immediately quenched to the room temperature. Temperature dependence of the dielectric constant as well as the dielectric loss was measured from −20 to 150 °C at the frequency ranging from 1 Hz to 1,000 kHz. The hysteresis loop was characterized by Radiant Workstation, and strain-electric field curve was measured by MTI Photonic Sensor at the frequency of 10 Hz.

## 3 Results and discussion

### 3.1 Structural characterizations

The relative density of all the samples, determined by Archimedes' method, are higher than 96 % of the theoretical density except the samples sintered below the 1,300 °C in route 1. The results of the XRD investigations for both the sample sintered at 1,320 °C and 1,400 °C by different routes are shown in Fig. 1. Obviously, the samples sintered at 1,320°C exhibited ferroelectric perovskite phases with the tetragonal structure, which can be characterized by the obvious splitting between (002) and (200) peaks. The c/a ratios were 1.0069 (BT + Mn) and 1.0087 [$BaTi_{(1-x)}Mn_xO_3$]. When sintered at 1,400 °C for 2 h, an obvious h-$BaTiO_3$ phase appeared only for the sample fabricated by route 1. These results indicated that the doping ways strongly affected the solubility of Mn ions into the $BaTiO_3$ lattice. Doping the manganese after the formation of the $BaTiO_3$ would result in the locally high concentration of manganese at the grain boundary and then result in the formation of h-$BaTiO_3$.

Figure 2a, b show the microstructures of the samples sintered in 1,320°C with different doping ways. For the BT + Mn sample, the grains were fine and uniform with average grain size of 1 μm, while the grains were also uniform but with coarse grains with average grain size of 7 μm in $BaTi_{(1-x)}Mn_xO_3$. The average grain sizes of all samples sintered from 1,300 to 1,400 °C are shown in Fig. 2c. It can be seen that grain growth was suppressed by the manganese doping after the calcinations of the $BaTiO_3$ powder (BT + Mn) in a wide range of sintering temperatures till turned to h-$BaTiO_3$ in 1,400 °C. For $BaTi_{(1-x)}Mn_xO_3$, it showed the uniform coarse grain all over the sintered temperatures from 1,300 to 1,400 °C, and the grain size were a gradual increase from 4 (1,300), 7 (1,320), 10 (1,350), 25 (1,380) to 38 μm (1,400 °C). For manganese-doped $BaTiO_3$, it is assumed that manganese ion is incorporated to the $Ti^{4+}$ site of the perovskite structure and any resulting deficiency in charge is compensated by oxygen vacancies. The grain growth would be promoted by the oxygen vacancies which contribute to the diffusion during the sintering [44]. However, in our SEM result in Fig. 2, the grain growth was inhibited in the manganese doping way of BT + Mn. It might be because of the dissolution of the manganese when the perovskite structure had been formed as well as inhibited the generation of oxygen vacancy. For the $BaTi_{(1-x)}Mn_xO_3$, the manganese can be incorporated to the $Ti^{4+}$ site easily by showing the uniform and coarse grain during the whole sinter temperatures. Hereafter, the experiments of the macroscopic properties were measured on these two kinds of samples sintered in the same temperature of 1,320 °C.

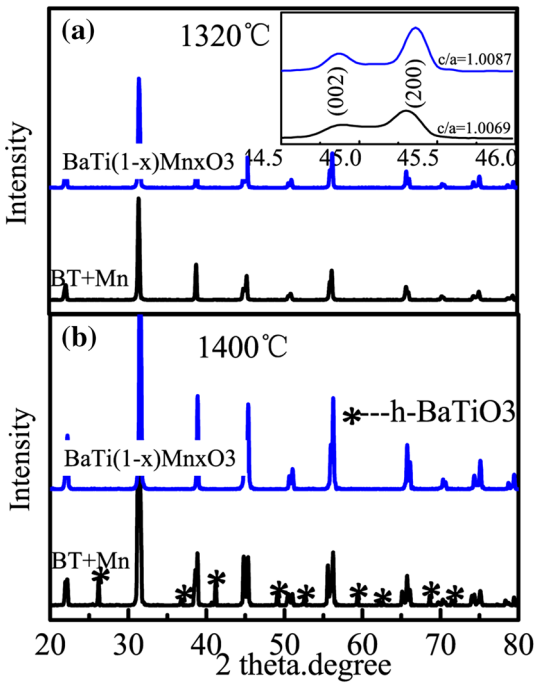


**Fig. 1** XRD patterns of samples sintered in **a** 1,320 °C and **b** 1,400 °C

### 3.2 Dielectric properties

The temperature dependence of the dielectric constant of the samples at 1 Hz to 1,000 kHz is shown in Fig. 3. For the two fabrication routes, they both showed a phase transition from ferroelectric to paraelectric phase in the curves of dielectric permittivity with same transition temperature of 125 °C. Apparent frequency dispersion was occurred in the entire measured temperature range in the BT + Mn sample. As shown in Fig. 3a, with the frequency increased from the 1 Hz to 1000 Hz, the dielectric constant were decreased especially in the $T_C$ from 8,000 to 4,200. The curve of the $BaTi_{(1-x)}Mn_xO_3$ showed almost no diffusion with the frequency, and the dielectric constant was nearly 9,500 at $T_C$. Moreover, the dielectric constant in the room temperature was quite different for the two fabrication routes, it decreased from nearly 3,000 (BT + Mn) to nearly 1,800 [BaTi(1−x)MnxO3] at the 1 Hz. The dielectric measurement shown in Fig. 3 demonstrated that doping the manganese into the $BaTiO_3$ powder result in the diffusion of the dielectric constant. It was attributed to the inhomogeneous distribution of the manganese at the grain boundary.

Figure 4 shows the frequency dependences of dielectric loss tan $\delta$ in ferroelectric phase at temperature range of 60–110 °C for the samples aged for 10 days and insets showed the curves of unaged samples. From the dielectric loss curves of BT + Mn sample shown in Fig. 4a, the relaxation type dielectric loss peaks moved to higher

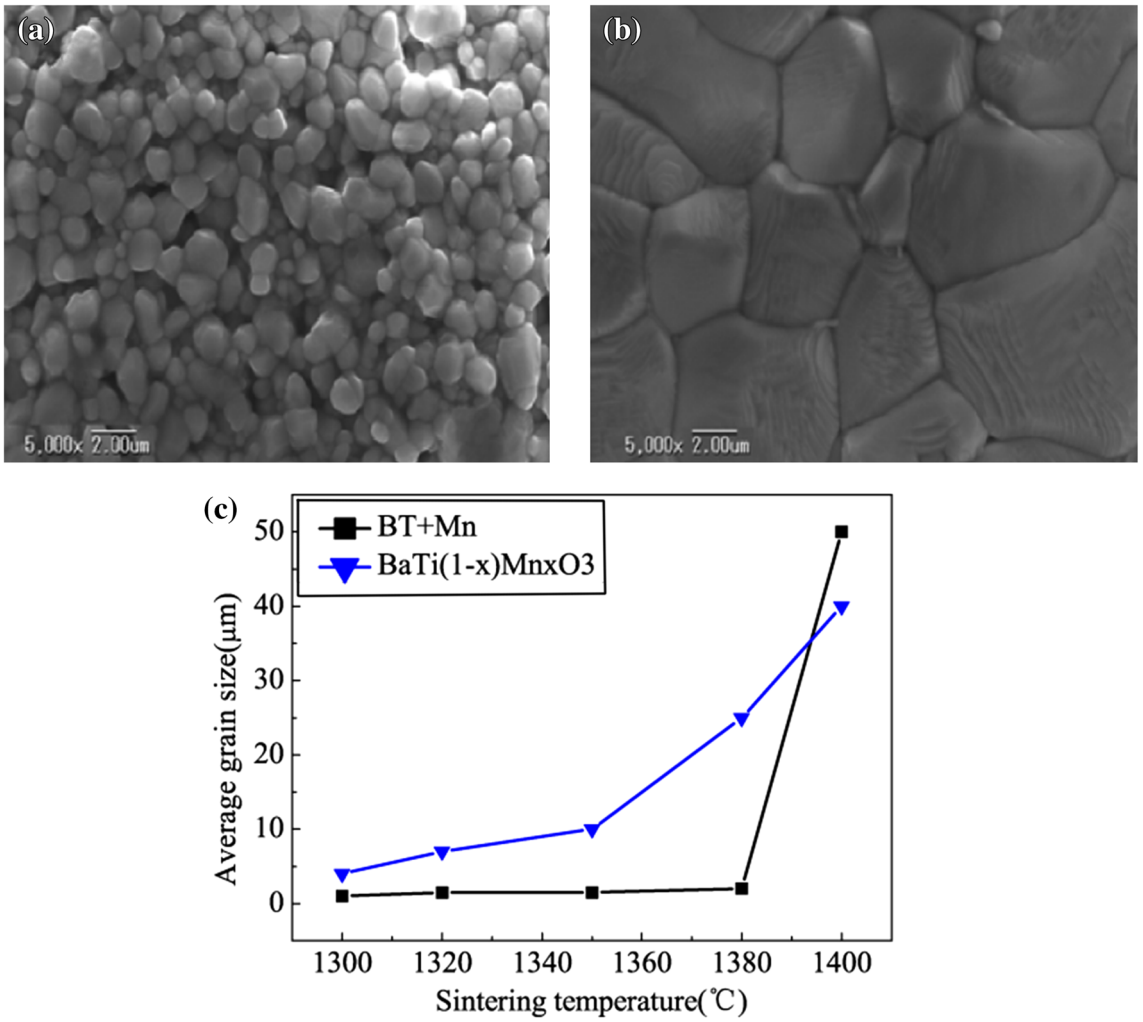


**Fig. 2** SEM of samples sintered in 1,320 °C by different doping ways of **a** BT + Mn and **b** $BaTi_{(1-x)}Mn_xO_3$. **c** The average grain size with sintered temperatures from 1,300–1,400 °C

frequency with the increasing of the temperatures can be obviously seen from the aged sample and the same as the unaged sample, but this peak has been weaken for the unaged one. As shown in Fig. 4b, an obviously relaxation peak was in the unaged samples for the $BaTi_{(1-x)}Mn_xO_3$, but disappeared after aging treatment. These observed relaxations were thermally activated phenomena, for which the characteristic activation energy can be deduced from the dielectric loss by the Arrhenius equation. According to the Arrhenius equation:

$$\tau = \tau_0 \exp\left(\frac{H}{\kappa T}\right), \tag{1}$$

where $T$ is the absolute temperature $\kappa$ is the Boltzmann's constant, $H$ is the activation energy and $\tau_0$ is the inverse of frequency factor. For a Debye peak, the condition for the peak is

$$\omega\tau = 1 \tag{2}$$

This gives:

$$\ln f = -\ln(2\pi\tau_0) - \frac{H}{\kappa T_p} \tag{3}$$

where $T_P$ and $f$ were the temperature and the frequency of the Debye peak. The Arrhenius plot is clearly shown in Fig. 4c. The BT + Mn sample showed the activation energy $H$ of 0.61 and 0.63 eV for the aged and the unaged samples. For the unaged $BaTi_{(1-x)}Mn_xO_3$ sample with $H$ of 0.55 eV, it was reported that there are two types of dielectric relaxation mechanism were proposed: space charge or long-range migration of oxygen vacancies which is applied at the high temperature and is characterized by the activation energies that range from 0.91 to 1.56 eV [45] and reorientation of oxygen vacancies in defect association [46–48]. It is a same research from the Cheng's studies that he attributed this dielectric loss relaxation peak observed in the ferroelectric phase to the reorientation of the electrical dipoles of $Co^{3+}$ and $V_o''$ [49].

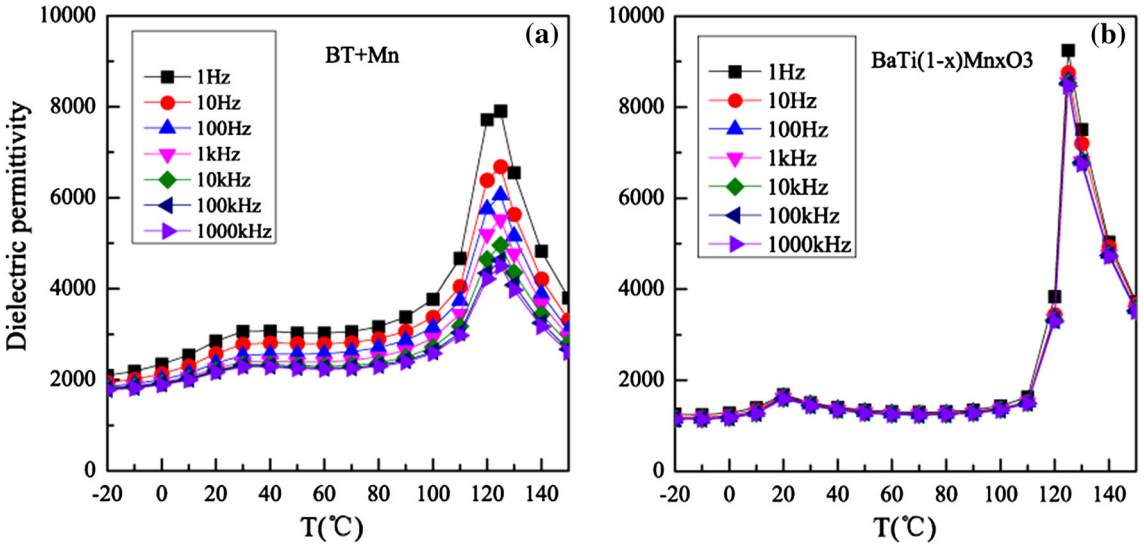


**Fig. 3** Temperature dependence of dielectric permittivity with doping ways of **a** BT + Mn and **b** $BaTi_{(1-x)}Mn_xO_3$ at the frequency of 1 Hz–1,000 kHz

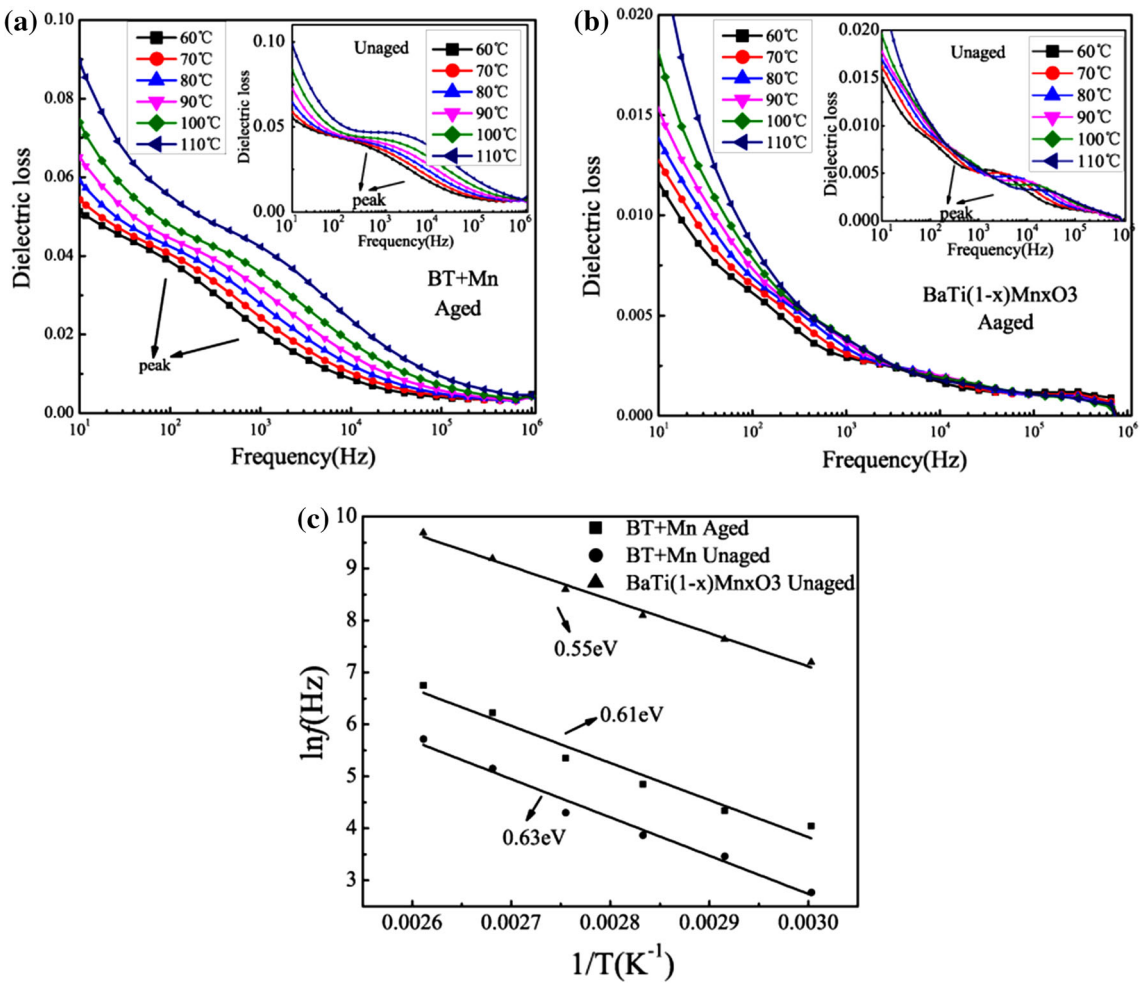


**Fig. 4** Frequency dependence of dielectric loss for aged samples **a** BT + Mn and **b** $BaTi_{(1-x)}Mn_xO_3$. The *insets* show the curves of the unaged samples. **c** The activation energies calculated by Arrhenius law

In our studies, we explained the dielectric loss relaxation shown in Fig. 4b by the volume effect model of ferroelectric aging, supported by Zhang and Ren [35–38]. According to their model, for the Mn-doped $BaTiO_3$, when immediately cooling the fresh sample through its ferroelectric phase, the crystal symmetry changes to the polar tetragonal symmetry, while oxygen vacancies surrounding a central $Mn^{3+}$ defect in the distorted oxygen octahedron retain their cubic symmetry, so it is not a stable state in the unaged sample. In order to be stable, the cubic defect symmetry will be corrected into a polar tetragonal one, which follows the crystal symmetry. Such process involves a short-range migration of oxygen vacancies. Therefore, the dielectric loss peak in Fig. 4b clearly shows this process of migration of oxygen vacancy; it is the process of the reorientation of an electric dipolar made of the oxygen vacancies and the $Mn^{3+}$. Moreover, after aging for 10 days, the relaxation peak disappeared was attribute to the nearly complete of the migration of oxygen vacancy as the defect symmetry in each domain follows the polar tetragonal crystal. As shown in Fig. 4c, the activation energy of the unaged $BaTi_{(1-x)}Mn_xO_3$ was 0.55 eV which was similar to the reported results of activation energy of oxygen vacancy diffusion of 0.44–0.68 eV [50] and the theoretical diffusion activation energy of the oxygen vacancies is 0.62 eV [51]. However, in the sample of BT + Mn, the dielectric loss relaxation peak was obviously even aged for 10 days. As shown in Fig. 4c, the

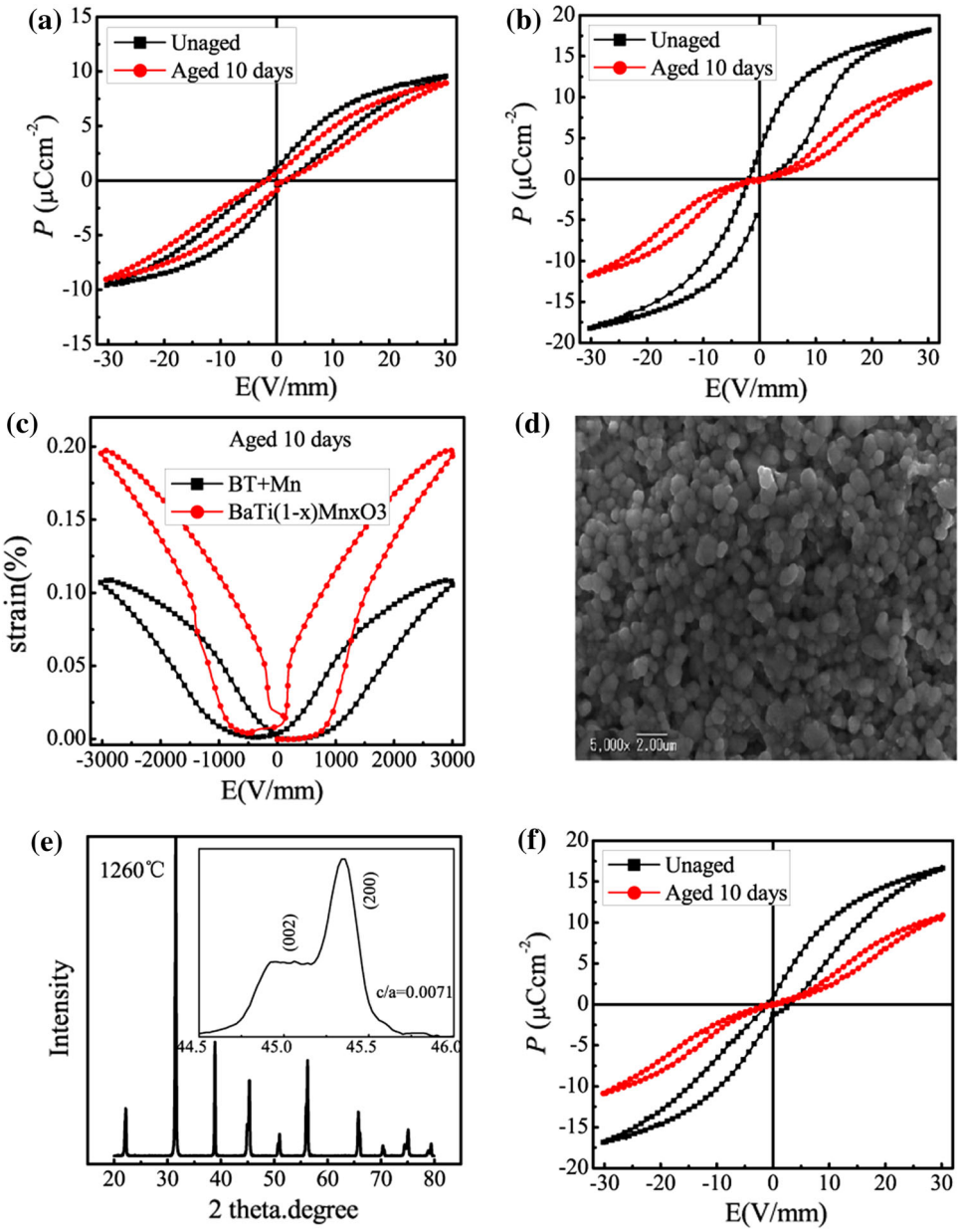


**Fig. 5** P-E loops of the sample aged and unaged for sample sintered at 1,320 °C **a** BT + Mn and **b** $BaTi_{(1-x)}Mn_xO_3$; **c**The recoverable electrostrain of the aged samples; **d** The SEM of the $BaTi_{(1-x)}Mn_xO_3$ sample sintered at 1,260 °C; **e** The XRD pattern of the $BaTi_{(1-x)}Mn_xO_3$ sample sintered at 1,260 °C; and **f** The P-E loops of the $BaTi_{(1-x)}Mn_xO_3$ sample sintered at 1,260 °C

dielectric loss relaxation behaviors were nearly the same in the unaged and aged samples. The activation energies were 0.61 and 0.63 eV which also could be attributed to the oxygen vacancy diffusion as well as the reorientation of the defect dipolar, but the amount of the oxygen vacancy was less and the more grain boundary battier impeded this process thus showed the higher activation energies.

### 3.3 Ferroelectric properties

Figure 5a shows the P-E loop of the BT + Mn sample unaged and aged for 10 days. Compared with the normal P-E loop in the unaged state, the P-E loop of the sample aged for 10 days showed a nearly normal P-E loop with a little constrict and decreased of the polarization, while the $BaTi_{(1-x)}Mn_xO_3$ sample that is shown in Fig. 5b showed the well constrictive double loop after aging treatment. As shown in Fig. 5c, the recoverable electrostrain of the two ways of doping samples increased from 0.11 % (BT + Mn) to 0.21 % [$BaTi_{(1-x)}Mn_xO_3$] at this sintering temperature. It can be explained by the Liu's studies [52] that large and homogeneous grains result in the large recoverable electrostrain and that the larger c/a ratio was another reason. From the research on the ferroelectric aging effect of dense $BaTi_{0.995}Mn_{0.005}O_3$ ceramics, the grain boundary barrier effect could result in the normal hysteresis loop in small grained samples even after the aging treatment [53]. Hence, we sintered the $BaTi_{(1-x)}Mn_xO_3$ ceramics at the 1,260 °C to get the sample with smaller grain size to find whether the fine grain size in the BT + Mn sample is the reason to inhibit the aging process. The microstructure of the $BaTi_{(1-x)}Mn_xO_3$ sample sintered at 1,260 °C is shown in Fig. 5d; average grain size of the sample was nearly 1 μm. The Fig. 5e shows the XRD pattern of this sample. The splitting between (002) and (200) peaks indicated its ferroelectric perovskite phases with the tetragonal structure, and the c/a ratio was 0.0071. Figure 5f shows the P-E loop of the samples in unaged and aged states. It can be seen that the obvious double loop attributed after aging. Thus, it illustrated that in the doping ways of $BaTi_{(1-x)}Mn_xO_3$, an obvious aging effect can be seen even with the fine grain. Moreover, it can be sure that the slight aging effect in the doping ways of BT + Mn was attributed to the dissolution of the manganese into the perovskite structure as well as difficultly formed of the more oxygen vacancy.

## 4 Conclusions

In the present study, the effect of fabrication routes on the microstructure, the dielectric and ferroelectric properties of the Mn-doped $BaTiO_3$ ceramics was systematically studied. It can be concluded that the ways of doping manganese into $BaTiO_3$ matrix had a strong impact on the obtained ceramics. Doping manganese after the calcination of $BaTiO_3$ (BT + Mn) would inhibit the grain growth and cause the hexagonal $BaTiO_3$ when sintered at 1,400 °C in the air. While doping manganese at the initial stage [$BaTi_{(1-x)}Mn_xO_3$], no hexagonal $BaTiO_3$ is detected in the same sintering temperature. As the macroscopic properties, the dielectric properties showed permittivity diffusion with the frequency in the temperature range of −10 to 150 °C only in the ceramics fabricated by the former route (BT + Mn). Moreover, the dielectric relaxation process disappeared after aging treatment only in the ceramics fabricated by the later route [$BaTi_{(1-x)}Mn_xO_3$]. The ferroelectric properties showed strong aging effect in the sample fabricated by the latter route [$BaTi_{(1-x)}Mn_xO_3$] both with fine grain and coarse grain, while the sample fabricated by the former route (BT + Mn) showed slight aging phenomenon ever after aging at room temperature for 10 days. The electrostrain also showed big difference within different samples: The recoverable electrostrain were 0.11 % (BT + Mn) and 0.21 % [$BaTi_{(1-x)}Mn_xO_3$] at the same sintering temperature of 1,320 °C and then aging in the room temperature for 10 days. The microstructure and the properties differences were attributed to the differences in solubility of manganese into the perovskite structure and so the generation of manganese–oxygen vacancy defect dipoles in the two doping ways.

**Acknowledgments** The authors thank W. F. Liu, C. Zhou and Y. Wang for helpful discussions.

## References

1. M. Rac, M. Chu, V. Ganine, Ceram. Trans. **100**, 1 (1999)
2. T.G. Reynold, Am. Ceram. Soc. Bull. **80**, 29 (2001)
3. I. Burn, J. Mater. Sci. **14**, 2453 (1979)
4. H.T. Langhammer, T. Miiller, A. Polity, K.H. Felgne, H.P. Abicht, Mater. Lett. **26**, 205 (1996)
5. A. Kirianov, N. Ozaki, H. Ohsato, N. Kohzu, H. Kishi, Jpn. J. Appl. Phys. **40**, 5619 (2001)
6. D.K. Lee, H.I. Yoo, K.D. Becker, Solid State Ionics **154**, 189 (2002)
7. B. Tang, S. Zhang, X. Zhou, Y. Yuan, J. Mater. Sci. Mater. Electron. **18**, 541 (2007)
8. Dennis P. Shay, Nikolas J. Podraza, Niall J. Donnelly, Clive A. Randall, J. Am. Ceram. Soc. **95**, 1348 (2012)
9. J. Jeong, Y.H. Han, J. Electroceram. **13**, 549 (2004)
10. S.I. Osawa, A. Furuzawa, N. Fujikawa, J. Am. Ceram. Soc. **76**, 1191 (1993)
11. W. Cai, C. Fu, G. Gao, X. Deng, J. Mater. Sci. Mater. Electron. **21**, 317 (2010)
12. S.H. Cha, Y.H. Han, J. Appl. Phys. **100**, 104102 (2006)
13. H. Moriwake, C.A.J. Fisher, A. Kuwabara, Jpn. J. Appl. Phys. **49**, 09MC01 (2010)
14. M.M. Vijatović Petrović, J.D. Bobić, R. Grigalaitis, B.D. Stojanović, J. Banys, Acta Phys. Pol. A **124**, 155 (2013)

15. J. Jaill, H.H. Young, J. Electroceram **13**, 549 (2004)
16. I. Burn, G.H. Maher, J. Mater. Sci. **10**, 633 (1975)
17. S.B. Desu, E.C. Subbarao, Adv. Ceram. **1**, 189 (1975)
18. J. Rödel, G. Tomandl, J. Mater. Sci. **19**, 3515 (1984)
19. F. Batllo, E. Duverger, J.-C. Jules, J.-C. Niepce, B. Jannot, M. Maglione, Ferroelectrics **109**, 113 (1990)
20. J. Illingsworth, H.M. Al-Allak, A.W. Brinkmann, J. Woods, J. Appl. Phys. **67**, 2088 (1990)
21. D.Y. Wang, K. Umeya, J. Am. Ceram. Soc. **74**, 280 (1991)
22. Y.-C. Chen, G.-M. Lo, C.-R. Shih, L. Wu, M.-H. Chen, K.-C. Huang, Jpn. J. Appl. Phys. **33**, 1412 (1994)
23. J. Illingsworth, H.M. AlAllak, A.W. Brinkman, J. Woods, J. Appl. Phys. **67**, 2088 (1990)
24. R. Waster, T. Baiatu, K.H. Härdtl, J. Am. Ceram. Soc. **73**, 1645 (1990)
25. S.H. Yoon, C.A. Randall, K.H. Hur, J. Am. Ceram. Soc. **93**, 1950 (2010)
26. R. Waster, R. Hagenbeck, Acta Mater. **48**, 797 (2000)
27. S. Sumita, M. Ikeda, Y. Nakano, K. Nishiyama, T. Nomura, J. Am. Ceram. Soc. **74**, 2739 (1991)
28. J.G. Dickson, L. Katz, R. Ward, J. Am. Chem. Soc. **83**, 3026 (1961)
29. L. Katz, R. Ward, Inorg. Chem. **3**, 205 (1964)
30. F. Ren, S. Ishida, S. Mineta, J. Ceram. Soc. Jpn. (Yogyo Kyokaishi) **102**, 106 (1994)
31. H.T. Langhammer, T. Müller, A. Polity, K.-H. Felgner, H.-P. Abicht, Mater. Lett. **26**, 205 (1996)
32. J. Weiss, G. Rosenstein, J. Mater. Sci. **23**, 3263 (1988)
33. I. Burn, J. Mater. Sci. **14**, 2453 (1979)
34. H.T. Langhammer, T. Müller, K.H. Felgner, H.P. Abicht, J. Am. Ceram. Soc. **83**, 605 (2000)
35. X. Ren, Nat. Mater. **3**, 91 (2004)
36. L.X. Zhang, W. Chen, X. Ren, Appl. Phys. Lett. **85**, 5658 (2004)
37. L.X. Zhang, X. Ren, Phys. Rev. B **71**, 174108 (2005)
38. L.X. Zhang, X. Ren, Phys. Rev. B **73**, 094121 (2006)
39. H.J. Hagemann, D. Hennings, J. Am. Ceram. Soc. **64**, 590 (1981)
40. J. Daniels, K.-H. Hardtl, D. Hennings, R. Wernicke, Philips Res. Rep. **31**, 487 (1976)
41. H. Kishi, N. Kohzu, Y. Iguchi, J. Sugino, M. Kato, H. Ohsato, T. Okuda, J. Eur. Ceram. Soc. **21**, 1643 (2001)
42. K. Albertsen, D. Hennings, O. Steigelmann, J. Electroceram. **2**, 193 (1998)
43. H. Gong, X.H. Wang, S.P. Zhang, H. Wen, L.T. Li, J. Eur. Ceram. Soc. **34**, 1733 (2014)
44. H.I. Hsiang, F.S. Yen, Y.H. Chang, J. Mater. Sci. **31**, 2417 (1996)
45. O. Bidault, P. Goux, M. Kchikech, M. Belkaoumi, M. Maglione, Phy. Rev. B **49**, 7868 (1994)
46. S.H. Cha, Y.H. Han, Jpn. J. Appl. Phys. **45**, 7797 (2006)
47. S.H. Cha, Y.H. Han, J. Appl. Phys. **100**, 104102 (2006)
48. W. Liu, C.A. Randall, J. Am. Ceram. Soc. **91**, 3245 (2008)
49. B.L. Cheng, J. Am. Ceram. Soc. **88**, 907 (2005)
50. G.V. Lewis, C.R.A. Catlow, R.E.W. Casslton, J. Am. Ceram. Soc. **68**, 555 (1985)
51. G.V. Lewis, C.R.A. Catlow, Radiat. Eff. Defects Solids **73**, 307 (1983)
52. W.F. Liu, L.X. Zhang, W. Chen, S.T. Li, J. Mater. Sci. Mater. Electron. **25**, 510 (2014)
53. Y.Y. Guo, Z.B. Yan, N. Zhang, W.W. Cheng, J.M. Liu, J. Mater. Sci. Mater. Electron. **107**, 243 (2012)